

## Full Length Article

Optoelectronic and photocatalytic properties of stable pentagonal B<sub>2</sub>S and B<sub>2</sub>Se monolayersNeha Katoch <sup>a,\*</sup>, Jagdish Kumar <sup>a</sup>, Ashok Kumar <sup>b,\*</sup>, P.K. Ahluwalia <sup>c</sup>, Ravindra Pandey <sup>d</sup><sup>a</sup> Department of Physics and Astronomical Science, School of Physical and Material Sciences, Central University of Himachal Pradesh, Dharamshala 176206, India<sup>b</sup> Department of Physics, School of Basic Sciences, Central University of Punjab, Bathinda, 151401, India<sup>c</sup> Department of Physics, Himachal Pradesh University, Shimla 171005, India<sup>d</sup> Department of Physics, Michigan Technological University, Houghton, MI 49931, USA

## ARTICLE INFO

## ABSTRACT

## Keywords:

DFT  
2D materials  
Optoelectronics  
Photocatalyst  
Pentagonal structures

Boron-based 2D monolayers have attracted tremendous interest due to their unique physical and chemical properties. In this paper, we report novel pentagonal monolayers, B<sub>2</sub>S and B<sub>2</sub>Se, which are predicted to be energetically, dynamically, and thermally stable based on density functional theory. At the HSE06 level of theory, they exhibit a moderate indirect bandgap of (e.g., 1.82 eV for Penta-B<sub>2</sub>S and 1.94 eV for Penta-B<sub>2</sub>Se). Strain-induced indirect-to-direct bandgap transition, high hole mobility ( $\sim 10^3 \text{ Cm}^2 \text{V}^{-1} \text{S}^{-1}$ ) and strong optical absorption ( $\alpha \sim 10^5 \text{ Cm}^{-1}$ ) in the visible region are observed for these monolayers. Moreover, the electronic band structures and optical spectra are tunable by mechanical strains suggesting their visible light-harvesting capabilities for optoelectronic applications. In this way, the pentagonal family of 2D materials is now expanded to include boron-containing photocatalytic materials for water splitting applications.

## 1. Introduction

Two-dimensional (2D) materials with pentagonal structures have generated great interest after the theoretical prediction of Penta-graphene [1]. Many efforts have been made to predict and synthesize pentagonal 2D materials theoretically and experimentally with interesting properties with a growing range of applications. Many 2D materials having pentagonal network such as Si-based Pentagonal monolayers [2], Penta-B<sub>2</sub>C [3], Penta-CN<sub>2</sub> [4], Penta-AlN<sub>2</sub> [5], Penta-BN<sub>2</sub> [6], Penta-BP<sub>5</sub> [7], Penta-NiS<sub>2</sub> [8], Penta-XS<sub>2</sub> (X = Ni, Pd, Pt) [9], Penta-BCN [10], Penta-NiX<sub>2</sub> (X = S, Se and Te) [11], and Penta-PtM<sub>2</sub> [12] etc. are theoretically predicted. Interestingly, in recent studies, Penta-PdSe<sub>2</sub> has been experimentally synthesized with high air stability (by mechanical exfoliation and chemical synthesis) [13-15]. These experimental studies mark a new hope for exploring pentagonal structures as a new family of 2D materials.

It is known that the properties of any material are correlated closely to the structures of the materials. Therefore, properties can be significantly modulated from unitary (Penta-graphene) to binary (Penta-PdSe<sub>2</sub>). For instance, unitary Penta-graphene has an intrinsic quasi-direct bandgap of 3.25 eV [1], superior ultrahigh strength, and is found to be suitable anode material for Li/Na-Ion batteries [16]. On the

other hand, binary Penta structures such as Penta-PdSe<sub>2</sub> can be used as a phototransistor [17], thermoelectric material [18], field-effect transistor [19] and photocatalyst for water splitting [20].

The wide and tunable bandgap of Penta-BP<sub>5</sub> has shown superior high-frequency-response to transition metal dichalcogenides (TMDs) and black phosphorus [7]. Other pentagonal structures such as Penta-BCN show high spontaneous polarization and prominent piezoelectricity, larger than the values associated with an h-BN sheet and functionalized Penta-graphene [1021]. Combining Penta-BN<sub>2</sub> with Penta-graphene vertically, the Schottky barrier becomes tunable for electronic applications [22]. Further, Penta-BN<sub>2</sub> has also been used as an anode material for Li-Ion batteries [23]. Recently, Penta-PC<sub>2</sub> being metallic, has shown an ultrahigh theoretical storage capacity for Li/Na absorption, greater than graphite [24]. On the other hand, Pentagonal PtTe<sub>2</sub> has a promising potential due to the significant thermoelectric response with a *zT* value of 5.03 along x-direction at 600 K [12]. Strain tunable solar cell power conversion efficiency of Penta-PdQ<sub>2</sub> (Q = S, Se) monolayers is predicted to be as high as 33.9% at the compressive strain of 5%. [25]. These attractive properties exhibited by pentagonal structures make them the potential candidates for future nanodevices.

The boron-based monolayer structures have received much attention in recent years [26-28]. The honeycomb monolayer B<sub>2</sub>S is a new

\* Corresponding authors.

E-mail addresses: [nehakatoch2@gmail.com](mailto:nehakatoch2@gmail.com) (N. Katoch), [ashokphy@cup.edu.in](mailto:ashokphy@cup.edu.in) (A. Kumar).

anisotropic Dirac cone material [29]. Recently, two-dimensional boron pnictides have shown photocatalytic behavior and suitable electronic and optical properties [30]. Our recent study has demonstrated excellent electronic and optical properties of boron-based hybrid monolayers, BX ( $X = \text{As, Sb, Bi}$ ) [31].

This study reports novel 2D Penta-B<sub>2</sub>S and Penta-B<sub>2</sub>Se monolayers using density functional theory (DFT). The stability of these monolayers is confirmed with phonon spectra and ab-initio molecular dynamics (AIMD) simulations. The influence of the uniaxial strain on the electronic and optical properties is also investigated. We have also explored the suitability of these monolayers under applied strain and varied pH of medium to be used as photocatalyst for water splitting.

## 2. Computational details

Density functional theory (DFT) based calculations have been performed using Vienna ab-initio Simulation Package (VASP) [32]. The electron-ion interactions are taken into account using the projector augmented wave (PAW) pseudo-potential method [33]. The cutoff for plane-wave kinetic energy and the convergence criterion of energy for self-consistent calculations have been set to be 600 eV and  $10^{-6}$  eV, respectively. At the DFT level, the generalized gradient approximation (GGA), in Perdew, Burke, and Ernzerhof (PBE) [34] parameterization, has been used to describe the exchange-correlation effects. The hybrid Heyd-Scuseria-Ernzerhof (HSE06) [35] functional is further used to calculate the electronic and optical properties. A well converged set of  $15 \times 15 \times 1$   $k$ -point mesh has been employed for Brillouin zone integrations. The structural relaxations are performed to force tolerance of  $10^{-6}$  eV/Å by computing the Hellmann-Feynman forces using the conjugate gradient algorithm. To ensure that the monolayers do not interact with their periodic images, a vacuum region of more than 10 Å along the z-axis is introduced.

To explore the dynamic stability, phonon dispersion spectra have been computed as implemented in the PHONOPY package [36], which employs the density functional perturbation theory (DFPT). To test the thermal stability of the studied monolayers, we performed AIMD calculations for 10000 fs with a time step of 1 fs using a canonical ensemble. The Nose algorithm [37] is used to control the temperature in

simulations. The optical properties have been studied by the sum over empty band states method [38]. A total of 64 bands have been used to calculate optical properties.

## 3. Results and discussion

The equilibrium configurations exhibiting a tetragonal lattice of Penta-B<sub>2</sub>S and Penta-B<sub>2</sub>Se are shown in Fig. 1(a, b). The results are similar to the previously reported results for Penta-graphene [1]. The top view reveals the formation of a Cairo pentagonal tiling pattern [39] constructed of pentagons, where each pentagon contains 4B and 2S or Se atoms. The buckled nature of these monolayers can be seen in the side view (Fig. 1(a, b)). The lattice constants of Penta-B<sub>2</sub>S and Penta-B<sub>2</sub>Se are calculated to be  $a = b = 4.49$  Å and 4.76 Å, respectively, are comparable to that of Penta-BP<sub>5</sub> [7]. Note that the lattice parameters of Penta-PdSe<sub>2</sub> are  $a = 5.75$  Å and  $b = 5.92$  Å [40]. The thickness of these monolayers is calculated as 1.32 Å (B<sub>2</sub>S) and 1.44 Å (B<sub>2</sub>Se). The structural parameters of these monolayers are listed in Table 1.

The chemical bonding in monolayer structures can be explained through the electron localization function (ELF) [41]. For example, the 1.0 ELF value shows complete localization of electrons, 0.5 shows full delocalization, and 0.0 represents the low charge density (Fig. 1(c, d)). Each B atom is coordinated with two S/Se atoms and one B atom, while each S/Se atom is coordinated with four B atoms and forms a pentagonal structure. The red region where the localization of electrons centers between the B-B and B-S (B-Se) bonds indicates covalent bonding in both monolayers. The localization of electrons between the B-B bonds is slightly larger than the B-S (B-Se) bonds indicating the stronger covalent bonding in B-B atoms. Also, the charge accumulation is found around the B atom, and depletion is around the S/Se atom (Fig. S1 of SI).

### 3.1. Stability

To check the energetic stability of the studied pentagonal structures, the cohesive energy per atom is calculated as:  $E_{coh} = (n_1 E_B + n_2 E_{S(\text{Se})} - E_{B_2S(B_2\text{Se})}) / (n_1 + n_2)$ , where,  $E_B$ ,  $E_{S(\text{Se})}$  and  $E_{B_2S(B_2\text{Se})}$  are the total energies of Boron, S (Se) atom of monolayers and Penta-B<sub>2</sub>S (Penta-B<sub>2</sub>Se) monolayer, respectively. Here  $n_1$  and  $n_2$  are the

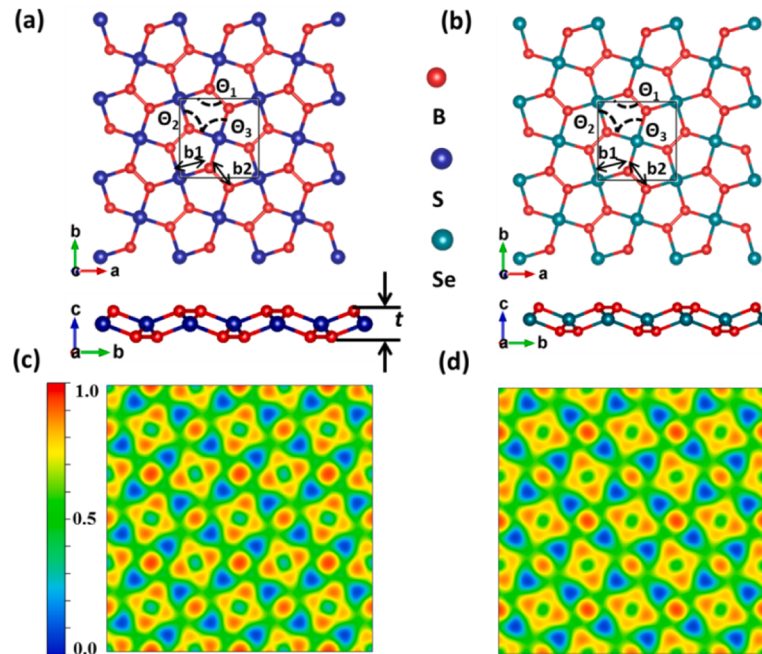


**Fig. 1.** Equilibrium structures with top and side views and ELF plots of Penta-B<sub>2</sub>S (a, c) and Penta-B<sub>2</sub>Se (b, d) monolayers.  $b1$  and  $b2$  are bond lengths between B and S/Se and B-B atoms, respectively.  $t$  is thickness.  $\Theta_1$ ,  $\Theta_2$ ,  $\Theta_3$  are the bond angles. Red, blue, and green balls denote the atoms of B, S, and Se.

**Table 1**

The calculated structural parameters of Penta-B<sub>2</sub>S and Penta-B<sub>2</sub>Se monolayers: lattice constant, thickness (t), bond lengths (b1, b2), bond angles ( $\Theta_1$ ,  $\Theta_2$  &  $\Theta_3$ ), cohesive energy ( $E_{coh}$ ) and bandgap ( $E_g$ ). For labeling the bond distances and bond angles, please see Fig. 1.

System	Lattice constant (Å)	t (Å)	Bond lengths (Å)		Bond angles (°)			$E_{coh}$ (eV/atom)	$E_g$ (eV)	
			b1	b2	$\Theta_1$	$\Theta_2$	$\Theta_3$		PBE	HSE
B <sub>2</sub> S	4.49	1.32	1.90	1.54	115.5	113.1	96.86	4.70	1.10	1.82
B <sub>2</sub> Se	4.76	1.44	2.04	1.54	116.5	110.6	97.14	4.35	1.23	1.94

number of Boron and S(Se) atoms, respectively. Cohesive energy for Penta-B<sub>2</sub>S (4.70 eV/atom) is higher than Penta-B<sub>2</sub>Se (4.35 eV/atom), indicating Penta-B<sub>2</sub>S is energetically more stable than Penta-B<sub>2</sub>Se. It is noted that the cohesive energies calculated for Penta-B<sub>2</sub>S and Penta-B<sub>2</sub>Se are similar to those of Penta-PdS<sub>2</sub> (4.71 eV) and Penta-PdSe<sub>2</sub> (4.30 eV) [25]. In addition to it, the calculated values of cohesive energies are comparable to those of the allotropes of arsenene [42], Boron-based hybrid monolayers [31], phosphorene [43,44], borophene [45], and honeycomb B<sub>2</sub>S monolayer [29].

To examine the dynamical stability of these monolayers, phonons spectra are calculated along the high symmetry directions in the first Brillouin zone using a  $4 \times 4 \times 1$  supercell (Fig. 2(a, b)). The absence of imaginary modes of lattice vibrations in the whole Brillouin zone indicates that both the studied monolayers are dynamically stable. In the band dispersion, the modes of vibrations are separated into low/high regimes of frequency by phonon gap. The acoustical in-plane phonon modes (longitudinal and transverse modes) have shown linear dispersion near  $\Gamma$ , whereas the out-of-plane modes have shown quadratic dispersion for both the monolayers. The slope of the acoustic out-of-plane modes near the  $\Gamma$  point is higher in Penta-B<sub>2</sub>S than Penta-B<sub>2</sub>Se.

We have further performed the AIMD simulations of these monolayers to examine their thermal stability. A  $3 \times 3 \times 1$  supercell for both monolayers is considered at temperature 500 K. The small fluctuations in temperature and energy curves are constant over almost 10000 fs time steps for both Penta-B<sub>2</sub>S and Penta-B<sub>2</sub>Se, as shown in Fig. 3. Also, the final structures of both the monolayers obtained at the end of simulations (insets of Fig. 3(b, d)) show negligible distortions supporting the thermal stability of these monolayers.

For completeness, we examine the trend in going from O to S to Se by considering Penta-B<sub>2</sub>O at the same level of theory. The calculated lattice parameter of Penta-B<sub>2</sub>O is  $a = b = 3.25$  Å, significantly less than that of Penta-B<sub>2</sub>S and Penta-B<sub>2</sub>Se monolayers (Table 1). This shortening of the lattice parameter is also reflected in the B-O bond distance, which is 1.58 Å. The B-B bond distance is 1.75 Å indicating the B-B bond to be weaker than the B-O bond in Penta-B<sub>2</sub>O. This is not the case with either B<sub>2</sub>S or B<sub>2</sub>Se, where the B-B bond is predicted to be stronger than B-S (B-Se) bond in the lattice (Table 1).

Interestingly, the phonon calculations find many imaginary modes of

lattice vibrations (Fig. S2 of SI), predicting the dynamical instability of the Penta-B<sub>2</sub>O monolayer. Thus, we believe that the weakening of the B-B bonds results in the predicted instability of Penta-B<sub>2</sub>O. Note that the boron clusters are highly reactive in interacting with O<sub>2</sub> [46], and the bulk B<sub>2</sub>O was shown to spontaneously decompose into borophene and B<sub>2</sub>O<sub>3</sub> by density functional theory calculations [47]. In the following discussion, we focus on the properties of Penta-B<sub>2</sub>S and Penta-B<sub>2</sub>Se monolayers.

### 3.2. Optoelectronic properties

Electronic band structure analysis reveals both Penta-B<sub>2</sub>S and Penta-B<sub>2</sub>Se to be indirect bandgap semiconductors with calculated indirect bandgaps of 1.1 eV (1.82 eV) and 1.23 eV (1.94 eV), respectively, along the M- $\Gamma$  direction, for PBE (HSE06) level of theory (Fig. 4). The quasi direct bandgaps along the  $\Gamma$ -X direction are found to be 1.35 eV (2.04) eV and 1.39 (2.05) eV for Penta-B<sub>2</sub>S and Penta-B<sub>2</sub>Se, respectively, using PBE (HSE06) level of theory. Note that, Penta-PdSe<sub>2</sub> is an indirect bandgap semiconductor with the experimentally measured optical bandgap 1.3 eV [48] and theoretical band gap is 1.39 eV [49].

The orbital projected band structures reveal that valence band maximum (VBM) in both monolayers mainly consists of B-p<sub>z</sub> states, whereas the conduction band minimum (CBM) shows mixed contributions from s-orbitals of B and S/Se atoms (Fig. S3 of SI). Also, the effect of spin-orbit coupling (SOC) on the electronic band structure of both Penta-B<sub>2</sub>S and Penta-B<sub>2</sub>Se is negligible (Fig. S4 of SI).

Next, we calculate the carrier mobilities of both Penta-B<sub>2</sub>S and Penta-B<sub>2</sub>Se following the phonon-limited scattering approach [50] at room temperature:

$$\mu = \frac{e\hbar^3 C}{K_B T |m^*|^2 E_{dp}^2} \quad (1)$$

Here,  $e$ ,  $\hbar$ ,  $K_B$ ,  $T$  and  $C$  are the electronic charge, reduced Plank's constant, temperature, and elastic modulus, respectively. The in-plane elastic modulus  $C$  can be calculated as follows:  $(E - E_0)/S_0 = C(\Delta l/l_0)^2/2$ , where  $E - E_0$ ,  $S_0$  and  $\Delta l/l_0$  are the total energy change, unit cell area, and deformations, respectively.  $m^*$  is the effective mass along the transport direction.  $E_{dp}$  is the deformation potential of electron (hole), which is given as the change in energy of the CBM and VBM w.r.t the applied compression and expansion to the unit cell.

The carrier mobilities for holes are calculated to be one order higher than electrons in both monolayers (Table 2). The higher mobilities for hole-type carriers can primarily be attributed to the hole's relatively small deformation potential (3.15 eV and 2.87 eV) compared to electrons (9.23 eV and 7.70 eV). Thus, considered Penta-B<sub>2</sub>S and Penta-B<sub>2</sub>Se monolayers seem to have hole-dominated transport. The obtained values for hole carrier mobilities for Penta-B<sub>2</sub>S and Penta-B<sub>2</sub>Se monolayers are less than that of Penta-PdSe<sub>2</sub> ( $1518 \text{ cm}^2 \text{V}^{-1} \text{s}^{-1}$ ) [25] but higher than that of h-BN ( $486.9 \text{ cm}^2 \text{V}^{-1} \text{s}^{-1}$ ) [51]. The calculated carrier mobilities are also comparable to the previously reported values for other 2D materials such as layered MoS<sub>2</sub> and WSe<sub>2</sub> [52].

To understand the optical behavior of these monolayers, we have calculated the absorption coefficient as:

$$\alpha(\omega) = \frac{\sqrt{2}\omega}{c} \left\{ [\epsilon_1^2(\omega) + \epsilon_2^2(\omega)]^{1/2} - \epsilon_1(\omega) \right\}^{1/2} \quad (2)$$

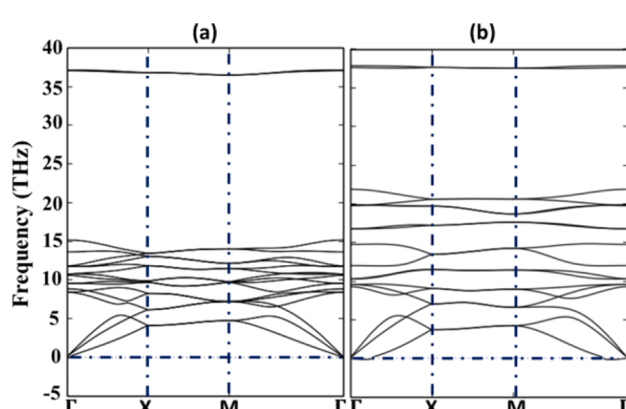
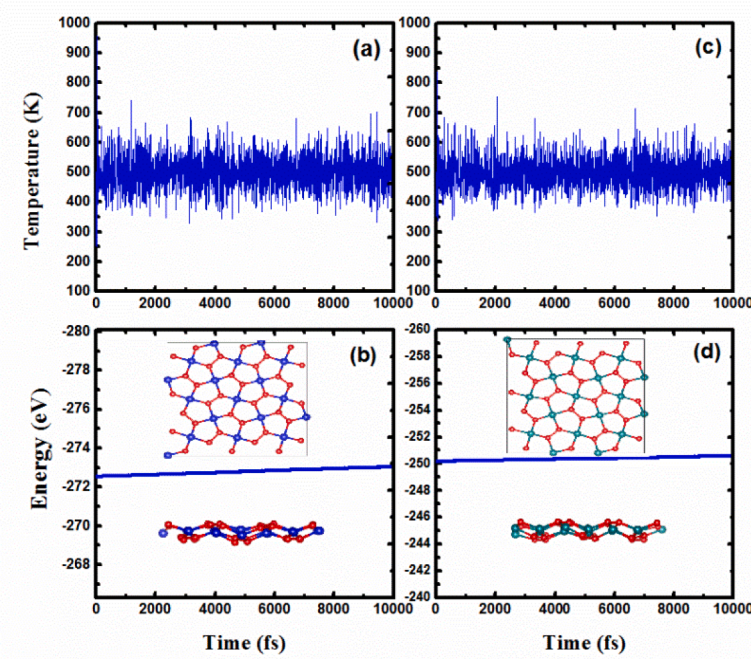
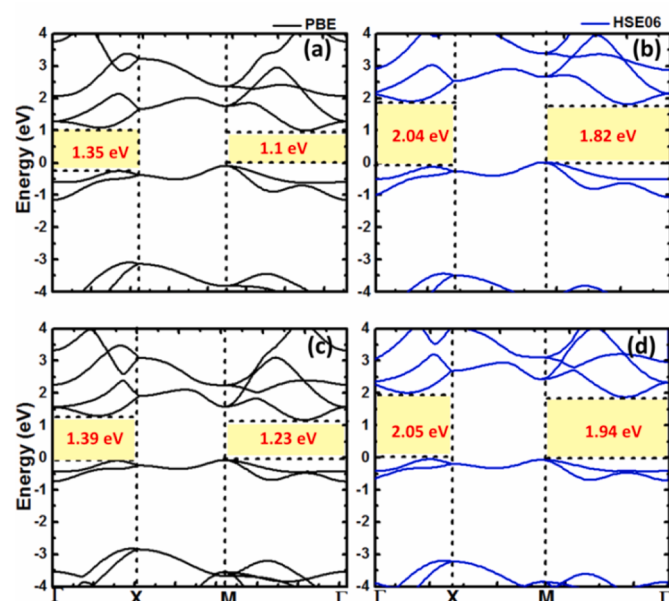


Fig. 2. Phonon dispersion relationship of (a) Penta-B<sub>2</sub>S and (b) Penta-B<sub>2</sub>Se monolayers.



**Fig. 3.** AIMD simulated curves for temperature and energy for Penta-B<sub>2</sub>S (a and b) and Penta-B<sub>2</sub>Se (c and d) at 500 K. Insets in (b) and (d) display the top and side views of final structures after 10000 fs in the lower panel.



**Fig. 4.** Electronic band structures of monolayers Penta-B<sub>2</sub>S (a and b) and Penta-B<sub>2</sub>Se (c and d) at PBE and HSE06 level of theory. The Fermi level is set at 0 eV.

where  $\epsilon_1$  and  $\epsilon_2$  are the real and imaginary part of the dielectric function [38,53,54]. Absorption coefficients for pristine monolayers of both Penta-B<sub>2</sub>S and Penta-B<sub>2</sub>Se are calculated to be  $\sim 10^5 \text{ cm}^{-1}$  for in-plane polarization and  $\sim 10^4 \text{ cm}^{-1}$  for out-of-plane polarization (Fig. 5(a, c) and (b, d)) by using HSE06. Absorption edge for pristine Penta-B<sub>2</sub>S and Penta-B<sub>2</sub>Se are calculated as 1.86 eV (1.92 eV) and 2.00 eV (1.96 eV), respectively, for in-plane (out-of-plane) polarization.

**Table 2**

The calculated elastic modulus ( $C$ ), effective mass ( $m^*$ ) for electron ( $m_e^*$ ) and holes ( $m_h^*$ ), deformation potential ( $E_{dp}$ ) and carrier mobility ( $\mu$ ) of Penta-B<sub>2</sub>S and Penta-B<sub>2</sub>Se monolayer.

Systems	Elastic modulus $C(Jm^{-2})$	Effective mass ( $m$ )		Deformation potential (eV)		Carrier mobility $Cm^2V^{-1}s^{-1}$	
		$m_e^*$	$m_h^*$	$E_{dp}^e$	$E_{dp}^h$	$\mu_e$	$\mu_h$
B <sub>2</sub> S	269.67	0.46	0.64	9.23	3.15	323	1434
B <sub>2</sub> Se	214.14	0.40	0.74	7.70	2.87	488	1026

Ongoing from Penta-B<sub>2</sub>S to Penta-B<sub>2</sub>Se there is blue shift of 0.14 eV (0.04 eV) in absorption edges for in-plane (out-of-plane) polarization.

The absorption spectrum can be widely tuned by applying mechanical strain (Fig. 5). For instance,  $\pm 5\%$  uniaxial strain in Penta-B<sub>2</sub>S and Penta-B<sub>2</sub>Se tune the absorption edge in the range of 1.76–2.00 eV (1.80–1.98 eV) and 1.70–2.07 eV (1.77–2.02 eV) for in-plane (out-of-plane) polarization. For both monolayers, the absorption edges for in-plane (out-of-plane) polarization are calculated in the visible region, suggesting the visible light-harvesting capabilities of these monolayers for photovoltaic applications. It is to be noted that the maximum absorption for Penta-PdSe<sub>2</sub> is found in the visible region [55]. Other Boron-based monolayers with indirect bandgaps, such as  $\beta$ -FeB<sub>6</sub> and  $\gamma$ -FeB<sub>6</sub> have shown absorption in the visible light region and are expected to be used in visible light-driven photocatalysis and solar harvesting process [56].

Next, we calculate the electron energy loss spectra (EELS) as:

$$EELS = Im \left( -\frac{1}{\epsilon(\omega)} \right) = \frac{\epsilon_2(\omega)}{\epsilon_1^2(\omega) + \epsilon_2^2(\omega)} \quad (3)$$

here  $\epsilon_1$  ( $\epsilon_2$ ) is a real (imaginary) part of the dielectric function.

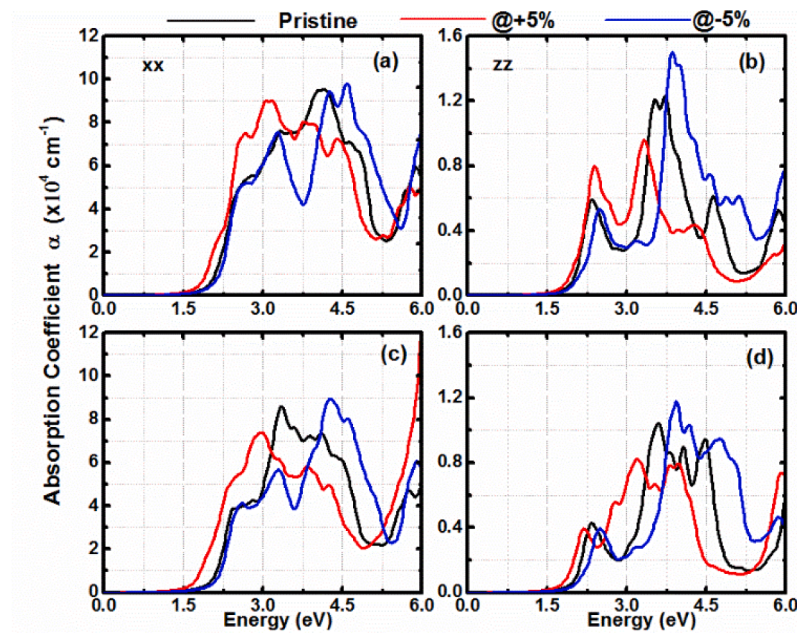


**Fig. 5.** The absorption spectra of pristine and  $\pm 5\%$  uniaxial strained (a, b) Penta-B<sub>2</sub>S and (c, d) Penta-B<sub>2</sub>Se at the HSE06 level of theory for in-plane (xx) polarization and out-of-plane (zz) polarization.

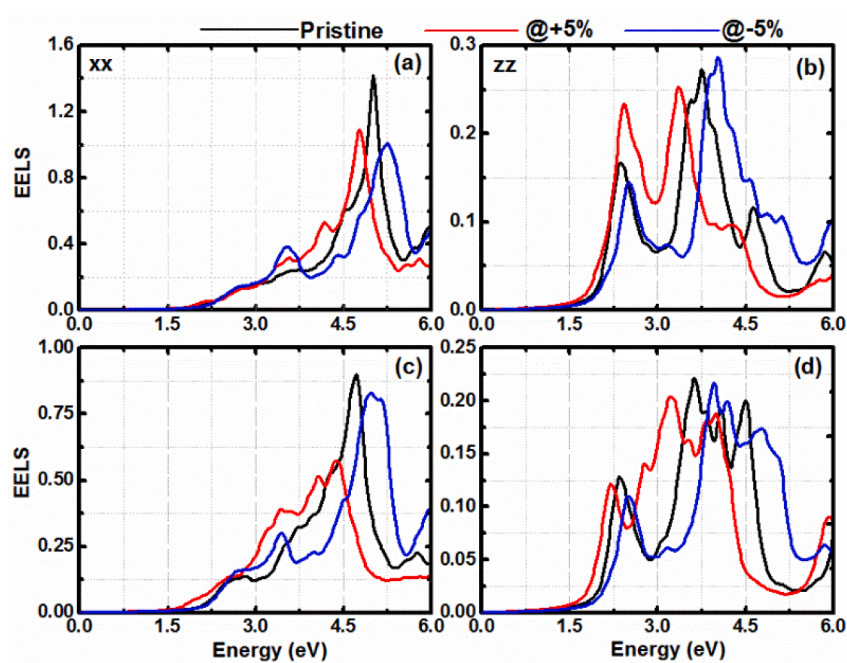


**Fig. 6.** The electron energy loss spectra (EELS) of pristine and  $\pm 5\%$  uniaxial strained (a, b) Penta-B<sub>2</sub>S and (c, d) Penta-B<sub>2</sub>Se at the HSE06 level of theory for in-plane (xx) polarization and out-of-plane (zz) polarization.

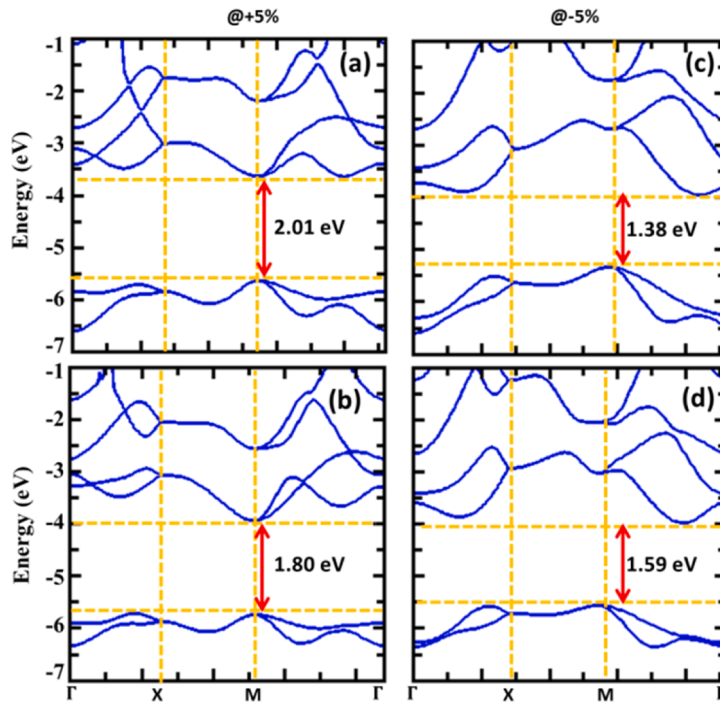


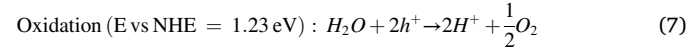
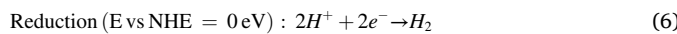
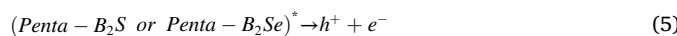
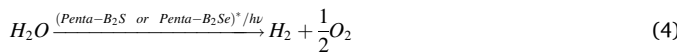
**Fig. 7.** Electronic band structure of Penta-B<sub>2</sub>S (**a** and **c**) and Penta-B<sub>2</sub>Se (**b** and **d**) monolayers at +5% and -5% uniaxial strains, at HSE06 level of theory. The yellow dashed horizontal lines indicate the band alignment of B<sub>2</sub>S and B<sub>2</sub>Se monolayers with respect to the vacuum level.

We found that the EELS is also tunable with uniaxial strain in both in-plane and out-of-plane polarization (Fig. 6). For instance, low-energy plasmonic excitation for Penta-B<sub>2</sub>S and Penta-B<sub>2</sub>Se for in-plane polarization can be tuned from ~4.8 eV to ~5.2 eV and ~4.4 eV to ~5.0 eV, respectively, at ±5% uniaxial strain (Fig. 6(a, c)).

Similarly, high-energy plasmonic excitations are tunable with mechanical strains (Fig. S6(a, c) of SI). The redshift in low-energy plasmonic excitation is noticed from Penta-B<sub>2</sub>S to Penta-B<sub>2</sub>Se monolayers for in-plane polarization. Note that the low energy plasmonic features are due to the  $\pi-\pi^*$  collective transitions, whereas high energy (>10 eV) plasmonic features are due to both  $\sigma-\sigma^*$  and  $\pi-\sigma^*$  collective transitions. The absorption spectra and EELS at a wide energy range are given in Figs. S5 and S6 of SI.

### 3.3. Photocatalytic properties

In this section, we present the feasibility of these monolayers for photocatalytic water splitting. Note that, for an efficient photocatalyst, the bandgap should be  $1.23\text{eV} < E_g < 3\text{eV}$ , and the band alignments should satisfy the condition of the redox potential of water [42,57–59]. The position of CBM (VBM) should be more positive (negative) than the redox potential of  $H_2/H^+$ ( $H_2O/O_2$ ) which is corresponding to the  $0\text{V}$  vs (NHE) ( $1.23\text{V}$  vs NHE). Note that NHE represents the normal hydrogen electrode. The process of water splitting reaction can be represented as [58]:



When the light of frequency larger than the bandgap falls on a given monolayer (Penta-B<sub>2</sub>S and Penta-B<sub>2</sub>Se), the electrons from the valance band get excited to the conduction band. If the energy of the holes which are present in the valence bands is larger than  $1.23\text{eV}(NHE)$  then they get united with the adsorbed water molecules and form  $H^+$  and  $O_2$  [60]. Consequently, the presence of Penta-B<sub>2</sub>S and Penta-B<sub>2</sub>Se in the excited state reduces the water molecule in hydrogen and oxygen molecules. To make Penta-B<sub>2</sub>S and Penta-B<sub>2</sub>Se monolayers suitable for water splitting, we have also looked into the influence of mechanical strains on the bandgaps and band alignments at different pH values. Such tuning of bandgaps by strain engineering is also achieved in experimental studies [61,62].

Both Penta-B<sub>2</sub>S and Penta-B<sub>2</sub>Se possess a bandgap larger than 1.23 eV. On applying the tensile uniaxial strain (+5%), an indirect-to-direct bandgap transition occurs for both the monolayers with bandgap values of 2.01 eV and 1.80 eV. With the compression strain (-5%), the bandgaps remain indirect, with values of 1.38 eV and 1.59 eV for Penta-B<sub>2</sub>S and Penta-B<sub>2</sub>Se (Fig. 7), respectively.

The position of CBM for both monolayers is more positive than the standard redox potentials at  $pH = 0$ , indicating the feasibility of reduction half-reaction. In contrast, the position of VBM for both the monolayers is less negative than the standard redox potentials (Fig. 7), indicating that the oxidation half-reaction at  $pH = 0$  is not possible. However, the standard redox potential is dependent on  $pH$  of the solution, where the standard oxidation potential in a solution is given as [60]:  $E_{O_2/H_2O} = 5.67\text{eV} - pH \times 0.059\text{eV}$ . Varied  $pH$  values of the solution lead to the equal shifting of oxidation and reduction potential [58]. Consequently, both Penta-B<sub>2</sub>S and Penta-B<sub>2</sub>Se possess favorable band positions for photocatalyst in neutral ( $pH = 7$ ) and basic ( $pH > 7$ ) medium (Fig. 8).

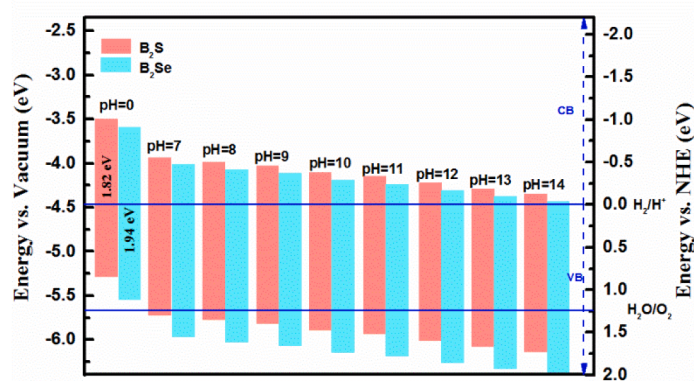


**Fig. 8.** Alignment of band energy of Penta-B<sub>2</sub>S and Penta-B<sub>2</sub>Se monolayers. Modulation of band alignment with different values of pH of the medium. Horizontal blue lines indicate the standard redox potential of water at pH = 0. CBM and VBM are shifted equally with the varied pH values.

Also, the band alignments of Penta-B<sub>2</sub>S and Penta-B<sub>2</sub>Se have been modified with both tensile and compression strains. The bands' alignments at  $\pm 5\%$  strain and different pH values are shown in Fig. S7 of SI, which indicates the tuning of photocatalytic properties of Penta-B<sub>2</sub>S and Penta-B<sub>2</sub>Se monolayers with mechanical strains and pH of the solution.

#### 4. Summary

The 2D pentagonal monolayers of B<sub>2</sub>S and B<sub>2</sub>Se are investigated using state-of-the-art density functional theory. These monolayers are energetically and thermodynamically stable, supporting their future experimental synthesis. These monolayers are indirect bandgap semiconductors showing the holes mobility one order higher than the electrons mobility. The application of uniaxial strains significantly modifies the electronic behavior of these monolayers, such as indirect-to-direct bandgap transition under the uniaxial expansion strain of  $+5\%$ . Absorption and electron energy loss spectra are tunable with  $\pm 5\%$  uniaxial strains in the visible region, making them good candidates for strain-tunable optoelectronic applications. Also, these monolayers exhibit suitable bandgaps and band edge positions for photocatalytic water splitting applications under suitable strains and solution conditions. These results make Penta-B<sub>2</sub>S and Penta-B<sub>2</sub>Se potential candidates for future devices at the nanoscale.

#### CRediT authorship contribution statement

**Neha Katoch:** Conceptualization, Software, Data curation, Investigation, Validation, Visualization, Writing – original draft, Writing – review & editing. **Jagdish Kumar:** Software, Conceptualization, Project administration, Supervision, Writing – review & editing. **Ashok Kumar:** Methodology, Conceptualization, Software, Visualization, Formal analysis, Writing – review & editing. **P.K. Ahluwalia:** Conceptualization, Resources, Writing – review & editing. **Ravindra Pandey:** Resources, Formal analysis, Writing – review & editing.

#### Declaration of Competing Interest

The authors declare that they have no known competing financial interests or personal relationships that could have appeared to influence the work reported in this paper.

#### Acknowledgments

N. Katoch gratefully acknowledges the fellowship provided by CUHP and National Param Supercomputing Facility at CDAC-Pune, which is utilized to obtain the results presented here. A high-performance computing cluster at Michigan Technological University is used to

obtain the MD simulation results presented in this paper.

#### Data Availability

The simulation data can be obtained on reasonable request.

#### Appendix A. Supplementary material

Supplementary data to this article can be found online at <https://doi.org/10.1016/j.commatsci.2022.111524>.

#### References

- [1] S. Zhang, J. Zhou, Q. Wang, X. Chen, Y. Kawazoe, P. Jena, Penta-graphene: a new carbon allotrope, Proc. Natl. Acad. Sci. U. S. A. 112 (8) (2015) 2372–2377, <https://doi.org/10.1073/pnas.1416591112>.
- [2] X. Li, Y. Dai, M. Li, W. Wei, B. Huang, Stable Si-based pentagonal monolayers: High carrier mobilities and applications in photocatalytic water splitting, J. Mater. Chem. A. 3 (47) (2015) 24055–24063, <https://doi.org/10.1039/C5TA05770A>.
- [3] F. Li, K. Tu, H. Zhang, Z. Chen, Flexible structural and electronic properties of a pentagonal B<sub>2</sub>C monolayer via external strain: a computational investigation, Phys. Chem. Chem. Phys. 17 (37) (2015) 24151–24156, <https://doi.org/10.1039/C5CP03885E>.
- [4] S. Zhang, J. Zhou, Q. Wang, P. Jena, Beyond graphitic carbon nitride: nitrogen-rich penta-CN<sub>2</sub> sheet, J. Phys. Chem. C. 120 (7) (2016) 3993–3998, <https://doi.org/10.1021/acs.jpcc.5b1251010.1021/acs.jpcc.5b12510.s001>.
- [5] J. Li, X. Fan, Y. Wei, H. Liu, S. Li, P. Zhao, G. Chen, Half-metallicity and ferromagnetism in penta-AlN<sub>2</sub> nanostructure, Sci. Rep. 6 (2016) 1–10, <https://doi.org/10.1038/srep33060>.
- [6] J. Li, X. Fan, Y. Wei, G. Chen, Penta-B<sub>x</sub> NY sheet: a density functional theory study of two-dimensional material, Sci. Rep. 6 (2016) 31840, <https://doi.org/10.1038/srep31840>.
- [7] S. Liu, B. Liu, B. Liu, X. Shi, J. Lv, S. Niu, M. Yao, Q. Li, R. Liu, T. Cui, Two-dimensional Penta-BP<sub>5</sub> sheets: high-stability, strain-tunable electronic structure and excellent mechanical properties, Sci. Rep. 7 (2017) 1–8, <https://doi.org/10.1038/s41598-017-02011-9>.
- [8] C.-T. Wang, S. Du, A unique pentagonal network structure of the NiS<sub>2</sub> monolayer with high stability and a tunable bandgap, Phys. Chem. Chem. Phys. 22 (14) (2020) 7483–7488, <https://doi.org/10.1039/DQCP00434K>.
- [9] H. Yang, Y. Li, Z. Yang, X. Shi, Z. Lin, R. Guo, L. Xu, H. Qu, S. Zhang, First-principles calculations of the electronic properties of two-dimensional pentagonal structure XS<sub>2</sub> (X = Ni, Pd, Pt), Vacuum 174 (2020) 109176, <https://doi.org/10.1016/j.vacuum.2020.109176>.
- [10] K. Zhao, Y. Guo, Y. Shen, Q. Wang, Y. Kawazoe, P. Jena, Penta-BCN: a new ternary pentagonal monolayer with intrinsic piezoelectricity, J. Phys. Chem. Lett. 11 (9) (2020) 3501–3506, <https://doi.org/10.1021/acs.jpclett.0c00824>.
- [11] S. Tang, S. Bai, M. Wu, D. Luo, J. Zhang, W. Sun, S. Yang, Low-cost pentagonal NiX<sub>2</sub> (X = S, Se, and Te) monolayers with strong anisotropy as potential thermoelectric materials, Phys. Chem. Chem. Phys. 24 (8) (2022) 5185–5198, <https://doi.org/10.1039/DICP05671A>.
- [12] W. Tao, Y. Zhao, Z. Zeng, X. Chen, H. Geng, Anisotropic thermoelectric materials: pentagonal PtM<sub>2</sub> (M = S, Se, Te), ACS Appl. Mater. Interfaces. 13 (2021) 8700–8709, <https://doi.org/10.1021/acsami.0c19460>.
- [13] A.D. Oyedele, S. Yang, L. Liang, A.A. Puretzky, K. Wang, J. Zhang, P. Yu, P. R. Pudasaini, A.W. Ghosh, Z. Liu, C.M. Rouleau, B.G. Sumpter, M.F. Chisholm, W. u. Zhou, P.D. Rack, D.B. Geohegan, K. Xiao, PdSe<sub>2</sub>: pentagonal two-dimensional

- layers with high air stability for electronics, *J. Am. Chem. Soc.* 139 (40) (2017) 14090–14097, <https://doi.org/10.1021/jacs.7b04865>.
- [14] E. Li, D. Wang, P. Fan, R. Zhang, Y.-Y. Zhang, G. Li, J. Mao, Y. Wang, X. Lin, S. Du, H.-J. Gao, Construction of bilayer PdSe<sub>2</sub> on epitaxial graphene, *Nano Res.* 11 (11) (2018) 5858–5865, <https://doi.org/10.1007/s12274-018-2090-0>.
- [15] S. Jiang, C. Xie, Y. Gu, Q. Zhang, X. Wu, Y. Sun, W. Li, Y. Shi, L. Zhao, S. Pan, P. Yang, Y. Huan, D. Xie, Q. Zhang, X. Liu, X. Zou, L. Gu, Y. Zhang, Anisotropic growth and scanning tunneling microscopy identification of ultrathin even-layered PdSe<sub>2</sub> ribbons, *Small* 15 (45) (2019) 1902789, <https://doi.org/10.1002/smll.201902789>.
- [16] B. Xiao, Y.-C. Li, X.-F. Yu, J.-b. Cheng, Penta-graphene: a promising anode material as the Li/Na-Ion battery with both extremely high theoretical capacity and fast charge/discharge rate, *ACS Appl. Mater. Interfaces* 8 (51) (2016) 35342–35352, <https://doi.org/10.1021/acsami.6b12727>.
- [17] T.S. Walmsley, K. Andrews, T. Wang, A. Haglund, U. Rijal, A. Bowman, D. Mandrus, Z. Zhou, Y.-Q. Xu, Near-infrared optical transitions in PdSe<sub>2</sub> phototransistors, *Nanoscale* 11 (30) (2019) 14410–14416, <https://doi.org/10.1039/C9NR03505B>.
- [18] Y. Zhao, P. Yu, G. Zhang, M. Sun, D. Chi, K. Hippalgaonkar, J.T.L. Thong, J. Wu, Low-symmetry PdSe<sub>2</sub> for high performance thermoelectric applications, *Adv. Funct. Mater.* 30 (52) (2020) 2004896, <https://doi.org/10.1002/adfm.202004896>.
- [19] W.L. Chow, P. Yu, F. Liu, J. Hong, X. Wang, Q. Zeng, C.H. Hsu, C. Zhu, J. Zhou, X. Wang, J. Xia, J. Yan, Y. Chen, D. Wu, T. Yu, Z. Shen, H. Lin, C. Jin, B.K. Tay, Z. Liu, High mobility 2D palladium diselenide field-effect transistors with tunable ambipolar characteristics, *Adv. Mater.* 29 (2017) 1–8, <https://doi.org/10.1002/adma.201602969>.
- [20] C. Long, Y. Liang, H. Jin, B. Huang, Y. Dai, PdSe<sub>2</sub>: flexible two-dimensional transition metal dichalcogenides monolayer for water splitting photocatalyst with extremely low recombination rate, *ACS Appl. Energy Mater.* 2 (1) (2019) 513–520, <https://doi.org/10.1021/acs.ame.8b01521>.
- [21] T. Thanasarnsurapong, K. Dabsamut, T. Maluangnont, J. T-Thienprasert, S. Junghawan, A. Boonchun, Piezoelectric and electronic properties of hydrogenated penta-BCN: a computational study, *J. Appl. Phys.* 129 (9) (2021) 095101, <https://doi.org/10.1063/5.0043450>.
- [22] K. Zhao, Y. Guo, Q. Wang, Contact properties of a vdW heterostructure composed of penta-graphene and penta-BN<sub>2</sub> sheets, *J. Appl. Phys.* 124 (16) (2018) 165103, <https://doi.org/10.1063/1.5047539>.
- [23] T. Zhang, Y. Ma, B. Huang, Y. Dai, Two-dimensional penta-BN<sub>2</sub> with high specific capacity for Li-Ion batteries, *ACS Appl. Mater. Interfaces* 11 (6) (2019) 6104–6110, <https://doi.org/10.1021/acsami.8b2056610.1021/acsami.8b20566.s001>.
- [24] W. Liu, X. Zu, Y. Zhou, H. Deng, Metallic two-dimensional penta-PC<sub>2</sub> structure with excellent electrical conductivity as superior anode material for both Li and Na ion batteries, *Appl. Surf. Sci.* 581 (2022) 152368, <https://doi.org/10.1016/j.apsusc.2021.152368>.
- [25] D. Raval, S.K. Gupta, P.N. Gajjar, R. Ahuja, Strain modulating electronic band gaps and SQ efficiencies of semiconductor 2D PdQ<sub>2</sub> (Q = S, Se) monolayer, *Sci. Rep.* 12 (2022) 1–13, <https://doi.org/10.1038/s41598-022-06142-6>.
- [26] C. Grazianetti, E. Cinquanta, A. Molle, A. Lherbier, A.R. Botello-méndez, J. Charlier, Electronic and optical properties of pristine and oxidized borophene, *2D Mater.* 3 (2016), 045006, <https://doi.org/10.1088/2053-1583/3/4/045006>.
- [27] B. Mortazavi, M. Makarem, M. Shahrokh, M. Raeisi, C.V. Singh, T. Rabczuk, L.F. C. Pereira, Borophene hydride: a stiff 2D material with high thermal conductivity and attractive optical and electronic properties, *Nanoscale* 10 (8) (2018) 3759–3768, <https://doi.org/10.1039/C7NR08725J>.
- [28] Y. Zhang, J. Kang, F. Zheng, P. Gao, S. Zhang, L. Wang, J. Kang, F. Zheng, P. Gao, S. Zhang, L. Wang, Borophosphene: a new anisotropic dirac cone monolayer with a high fermi velocity and a unique self-doping feature, *J. Phys. Chem. Lett.* 10 (2019) 6656–6663, <https://doi.org/10.1021/acs.jpclett.9b02599>.
- [29] Y. Zhao, X. Li, J. Liu, C. Zhang, Q. Wang, A new anisotropic dirac cone material: a B<sub>2</sub>S honeycomb monolayer, *J. Phys. Chem. Lett.* 9 (7) (2018) 1815–1820, <https://doi.org/10.1021/acs.jpclett.8b00616>.
- [30] H. Shu, J. Guo, X. Niu, Electronic, photocatalytic, and optical properties of two-dimensional boron pnictides, *J. Mater. Sci.* 54 (3) (2019) 2278–2288, <https://doi.org/10.1007/s10853-018-2987-8>.
- [31] N. Katoch, A. Kumar, J. Kumar, P.K. Ahluwalia, R. Pandey, Electronic and optical properties of boron-based hybrid monolayers, *Nanotechnology*, 32 (41) (2021) 415203, <https://doi.org/10.1088/1361-6528/ac0e69>.
- [32] G. Kresse, J. Furthmüller, Efficient iterative schemes for ab initio total-energy calculations using a plane-wave basis set, *Phys. Rev. B - Condens. Matter Mater. Phys.* 54 (16) (1996) 11169–11186, <https://doi.org/10.1103/PhysRevB.54.11169>.
- [33] P.E. Blöchl, Projector augmented-wave method, *Phys. Rev. B* 50 (24) (1994) 17953–17979, <https://doi.org/10.1103/PhysRevB.50.17953>.
- [34] J.P. Perdew, J.A. Chevary, S.H. Vosko, K.A. Jackson, M.R. Pederson, D.J. Singh, C. Fiolhais, Erratum atoms, molecules, solids, and surfaces: applications of the generalized gradient approximation for exchange and correlation, *Phys. Rev. B* 48 (7) (1993) 4978, <https://doi.org/10.1103/PhysRevB.48.4978.2>.
- [35] J. Heyd, G.E. Scuseria, Efficient hybrid density functional calculations in solids: assessment of the Heyd-Scuseria-Ernzerhof screened Coulomb hybrid functional, *J. Chem. Phys.* 121 (3) (2004) 1187–1192, <https://doi.org/10.1063/1.1760074>.
- [36] A. Togo, I. Tanaka, Scripta Materialia First principles phonon calculations in materials science, *Scr. Mater.* 108 (2015) 1–5, <https://doi.org/10.1016/j.scriptamat.2015.07.021>.
- [37] S. Nosé, A unified formulation of the constant temperature molecular dynamics methods, *J. Chem. Phys.* 81 (1) (1984) 511–519, <https://doi.org/10.1063/1.447334>.
- [38] M. Gajdoš, K. Hummer, G. Kresse, J. Furthmüller, F. Bechstedt, Linear optical properties in the projector-augmented wave methodology, *Phys. Rev. B* 73 (4) (2006), <https://doi.org/10.1103/PhysRevB.73.045112>.
- [39] E. Ressouche, V. Simonet, B. Canals, M. Gospodinov, V. Skumryev, Magnetic frustration in an iron-Based cairo pentagonal lattice, *Phys. Rev. Lett.* 103 (2009) 1–4, <https://doi.org/10.1103/PhysRevLett.103.267204>.
- [40] D. Qin, P. Yan, G. Ding, X. Ge, H. Song, G. Gao, Monolayer PdSe 2: a promising two-dimensional thermoelectric material, *Sci. Rep.* 8 (2018) 2764, <https://doi.org/10.1038/s41598-018-20918-9>.
- [41] A.D. Becke, K.E. Edgecombe, A simple measure of electron localization in atomic and molecular systems A simple measure of electron localization in atomic and molecular systems, *J. Chem. Phys.* 92 (9) (1990) 5397–5403, <https://doi.org/10.1063/1.458517>.
- [42] P. Jamdaghi, A. Thakur, A. Kumar, P.K. Ahluwalia, R. Pandey, Two dimensional allotropes of arsenene with a wide range of high and anisotropic carrier mobility, *Phys. Chem. Chem. Phys.* 20 (47) (2018) 29939–29950, <https://doi.org/10.1039/C8CP06162A>.
- [43] W. Hu, J. Yang, Defects in phosphorene, *J. Phys. Chem. C* 119 (35) (2015) 20474–20480, <https://doi.org/10.1021/acs.jpcc.5b06077>.
- [44] C. Wang, Y. You, J.-H. Choi, First-principles study of defects in blue phosphorene, *Mater. Res. Express.* 7 (1) (2020) 015005, <https://doi.org/10.1088/2053-1591/ab59fc>.
- [45] P. Hess, Bonding, structure, and mechanical stability of 2D materials: the predictive power of the periodic table, *Nanoscale Horiz.* 6 (11) (2021) 856–892, <https://doi.org/10.1039/DNH00113B>.
- [46] W.J. Slough, A.K. Kandalam, R. Pandey, Reactivity of neutral and charged B<sub>13</sub> clusters with O<sub>2</sub>: a theoretical study, *J. Chem. Phys.* 132 (10) (2010) 104304, <https://doi.org/10.1063/1.3336404>.
- [47] F.M. Arnold, G. Seifert, J. Kunstmänn, Thermodynamic stability of borophene, B<sub>2</sub>O<sub>3</sub> and other B<sub>1-x</sub>O<sub>x</sub> sheets, *J. Phys. Commun.* 4 (3) (2020) 031001, <https://doi.org/10.1088/2399-6528/ab7a76>.
- [48] G. Zhang, M. Amani, A. Chaturvedi, C. Tan, J. Bullock, X. Song, H. Kim, D.-H. Lien, M.C. Scott, H. Zhang, A. Javey, Optical and electrical properties of two-dimensional palladium diselenide Optical and electrical properties of two-dimensional palladium diselenide, *Appl. Phys. Lett.* 114 (25) (2019) 253102, <https://doi.org/10.1063/1.5097825>.
- [49] M. Jakhar, J. Singh, A. Kumar, K. Tankeshwar, Pressure and electric field tuning of van der Waals heterostructure, *Nanotechnology* 31 (2020), 145710, <https://doi.org/10.1088/1361-6528/ab5de1>.
- [50] J. Bardeen, W. Shockley, Deformation potentials and mobilities in non-polar crystals, *Phys. Rev.* 80 (1) (1950) 72–80, <https://doi.org/10.1103/PhysRev.80.72>.
- [51] S. Bruzzone, G. Fiori, Ab-initio simulations of deformation potentials and electron mobility in chemically modified graphene and two- dimensional hexagonal boron-nitride, *Appl. Phys. Lett.* 99 (22) (2011) 222108, <https://doi.org/10.1063/1.3665183>.
- [52] D. Akinwande, N. Petrone, J. Hone, Two-dimensional flexible nanoelectronics, *Nat. Commun.* 5 (2014) 1–12, <https://doi.org/10.1038/ncomms6678>.
- [53] F. Wooten, *Optical Properties of Solids*, Academic Press, New York, 1972.
- [54] M. Fox, *Optical Properties of Solids*, Oxford University Press, 2001.
- [55] M. Jakhar, J. Singh, A. Kumar, R. Pandey, First-principles study of the hexagonal T-phase PdSe<sub>2</sub> monolayer and its application in solar cells, *J. Phys. Chem. C* 124 (49) (2020) 26565–26571, <https://doi.org/10.1021/acs.jpcc.0c05632>.
- [56] H. Zhang, Y. Li, J. Hou, K. Tu, Z. Chen, FeB<sub>6</sub> monolayers: the graphene-like material with hypercoordinate transition metal, *J. Am. Chem. Soc.* 138 (17) (2016) 5644–5651, <https://doi.org/10.1021/jacs.6b0176910.1021/jacs.6b01769.s001>.
- [57] U. Gupta, C.N.R. Rao, Hydrogen generation by water splitting using MoS<sub>2</sub> and other transition metal dichalcogenides, *Nano Energy* 41 (2017) 49–65, <https://doi.org/10.1016/j.nanoen.2017.08.021>.
- [58] S. Kaur, A. Kumar, S. Srivastava, K. Tankeshwar, R. Pandey, Monolayer, and heterostructures of green phosphorene for water splitting and photovoltaics, *J. Phys. Chem. C* 122 (45) (2018) 26032–26038, <https://doi.org/10.1021/acs.jpcc.8b08566>.
- [59] P. Jamdaghi, R. Pandey, K. Tankeshwar, First principles study of Janus WSe<sub>Te</sub> monolayer and its application in photocatalytic water splitting, *Nanotechnolo.* 33 (2) (2022) 025703, <https://doi.org/10.1088/1361-6528/ac2d46>.
- [60] X. Lv, W. Wei, Q. Sun, F. Li, B. Huang, Y. Dai, Two-dimensional germanium monochalcogenides for photocatalytic water splitting with high carrier mobility, *Appl. Catal. B Environ.* 217 (2017) 275–284, <https://doi.org/10.1016/j.apcatb.2017.05.087>.
- [61] J. Feng, X. Qian, C.-W. Huang, J. Li, Strain-engineered artificial atom as a broad-spectrum solar energy funnel, *Nat. Photonics* 6 (12) (2012) 866–872, <https://doi.org/10.1038/nphoton.2012.285>.
- [62] B. Sa, Y.-L. Li, J. Qi, R. Ahuja, Z. Sun, Strain engineering for phosphorene: the potential application as a photocatalyst, *J. Phys. Chem. C* 118 (46) (2014) 26560–26568, <https://doi.org/10.1021/jp508618t>.